

See discussions, stats, and author profiles for this publication at: <https://www.researchgate.net/publication/40755761>

Anharmonicities and Isotopic Effects in the Vibrational Spectra of X-center dot H₂O, center dot HDO, and center dot D₂O [X = Cl, Br, and I] Binary Complexes

ARTICLE in THE JOURNAL OF PHYSICAL CHEMISTRY A · DECEMBER 2009

Impact Factor: 2.69 · DOI: 10.1021/jp9088782 · Source: PubMed

CITATIONS

20

READS

38

6 AUTHORS, INCLUDING:



Samantha Horvath

Illinois Rocstar LLC

20 PUBLICATIONS 249 CITATIONS

SEE PROFILE



Ben M. Elliott

University of California, Los Angeles

23 PUBLICATIONS 336 CITATIONS

SEE PROFILE



Joseph R Roscioli

Aerodyne Research, Inc.

45 PUBLICATIONS 1,446 CITATIONS

SEE PROFILE

Anharmonicities and Isotopic Effects in the Vibrational Spectra of $X^- \cdot H_2O$, $\cdot HDO$, and $\cdot D_2O$ [$X = Cl, Br$, and I] Binary Complexes[†]

Samantha Horvath and Anne B. McCoy*

Department of Chemistry, The Ohio State University, Columbus, Ohio 43210

Ben M. Elliott, Gary H. Weddle, Joseph R. Roscioli, and Mark A. Johnson*

Sterling Chemistry Laboratory, Yale University, P.O. Box 208107, New Haven, Connecticut 06520

Received: September 14, 2009; Revised Manuscript Received: October 29, 2009

Vibrational predissociation spectra of the argon-tagged halide monohydrates, $X^- \cdot H_2O \cdot Ar$ ($X = Cl, Br$, or I), are recorded from ~ 800 to 3800 cm^{-1} by monitoring the loss of the argon atom. We use this set of spectra to investigate how the spectral signatures of the hydrogen-bonding and large-amplitude hindered rotations of the water molecule are affected by incremental substitution of the hydrogen atoms by deuterium. All six vibrational modes of the $X^- \cdot H_2O$ complexes are assigned through fundamental transitions, overtones, or combination bands. To complement the experimental study, harmonic and reduced-dimensional calculations of the vibrational spectra are performed based on the MP2/aug-cc-pVTZ level of theory and basis set. Comparison of these results with those from the converged six-dimensional calculations of Rheinecker and Bowman [*J. Chem. Phys.* **2006**, *125*, 133206.] show good agreement, with differences smaller than 30 cm^{-1} . The simpler method has the advantage that it can be readily extended to the heavier halides and was found to accurately recover the wide range of behaviors displayed by this series, including the onset of tunneling between equivalent minima arising from the asymmetrical (single ionic hydrogen-bonded) equilibrium structures of the complexes.

I. Introduction

Although the identification of hydrated halides as independent species is a central concept in aqueous electrolyte chemistry,¹ the molecular-level nature of the interactions has only recently been unveiled as experimental and theoretical tools have finally become equal to the challenge of accurately treating them. Examples where such knowledge is critical include the theoretical treatment of the heterogeneous chemistry of aerosol particles^{2–5} and the transport of ions across channels in biological membranes.^{6,7} The modeling of such complex systems at finite temperatures often relies on the use of interaction potentials,^{8–10} and these potentials are, in turn, derived from a detailed analysis of the elementary binary interaction between the water molecule and the ion.¹¹

In recent years, several reports have described the analysis of the vibrational structure arising from halide–water complexes using the “messenger” atom technique,^{12–21} which can now be carried out with sufficient spectral coverage to identify vibrational transitions associated with five of the six expected normal modes. A significant aspect of this effort is the observation of a variety of strong anharmonic effects that give rise to many more bands than are predicted based on the calculated vibrational spectrum within the usual harmonic oscillator and linear dipole approximations.

From a molecular physics perspective, these extra transitions are quite useful. Their presence reveals the strength and nature of the coupling between the modes and the coordinate dependence of the electric dipole moment surface. The variety of anharmonicities observed include Fermi resonances, combina-

tion bands, and overtone transitions arising from both distorted potential curves as well as intracomplex charge transfer.^{14,15,19,22}

In a recent paper,¹⁵ we discussed the spectral signatures associated with the vibrations arising from a proton that is hydrogen-bonded to a variety of anions; here, we focus on the implications of the spectra on the lower-energy motions arising from frustrated rotation of the water molecule against the ion. We accomplish this by analyzing a comprehensive data set involving the Cl^- , Br^- , and I^- ions combined with three isotopic variations of the water molecule (H_2O , HDO , and D_2O). We are particularly interested in exploring the behavior of the in-plane (ip) and out-of-plane (oop) bending modes.

The equilibrium geometry of the halide–water complexes can be described as an asymmetric (single ionic hydrogen-bonded) structure with the general arrangement depicted in Figure 1A. One important finding of the extensive earlier studies^{15,23} was the unexpectedly large intensity in the overtone transition in the oop bend ($2\nu_{oop}$). In $Cl^- \cdot H_2O$ and $Br^- \cdot H_2O$, the intensity of the overtone in the oop bend was found to be almost equal to that of the fundamental in the water bend (ν_{HOH}). In our analysis of this band, we were surprised to find that a one-dimensional description of this vibration described not only the frequencies of these transitions but also their unexpectedly large intensities, which were attributed to electrical anharmonicities (i.e., the shape of the electric dipole moment surface). Here, we follow the evolution of these effects upon all possible deuterations of the water molecule to effectively change the range of the surface explored by the overtone and thus better quantify the dominant cause of the anomalous overtone intensities.

The minimum-energy structure displayed in Figure 1A is, of course, one of two equivalent structures that are separated by a

[†] Part of the “W. Carl Lineberger Festschrift”.

* Authors to whom correspondence should be addressed.

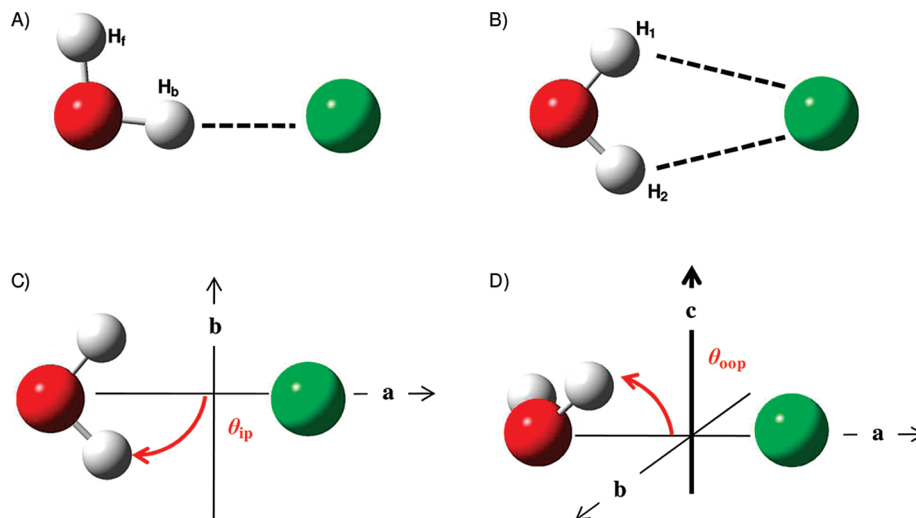


Figure 1. $X^- \cdot H_2O$ structures. In (A) and (B), the two low-energy stationary points are shown, with (A) providing the minimum-energy structure with C_s symmetry and (B) the C_{2v} transition-state structure. Panels (C) and (D) show the definitions of the ip (θ_{ip}) and oop bend coordinates (θ_{oop}). a , b , and c represent the three inertial axes.

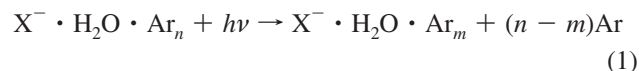
low-lying saddle point with C_{2v} symmetry, shown in Figure 1B. The ip bend, which can be thought of as the frustrated rotation of the water molecule about its c inertial axis, is the coordinate that connects these minima and leads to exchange of the hydrogen atoms in the double-minimum potential. Experimentally, this is the least accessible motion of the six normal modes, and its activity has only been tentatively identified through a combination band involving one quantum in the ip bend and one quantum in the water bend in the $Cl^- \cdot H_2O$ system in ref 15.

In this paper, we extend the spectroscopic studies to follow the dependence of this putative combination band on partial and full deuteration and on the strength of the $X^- \cdot H_2O$ interaction in the $X = Cl, Br$, and I systems. Particularly interesting aspects regarding the behavior of the ip bend are the role of tunneling splitting and the question of whether transitions involving overtones in the ip bend display similar intensity anomalies as those observed in transitions based on the oop bend vibration. Given that these transitions are likely to only be observed as combination bands, this raises the issue of how well the spectra of these complexes are described by a series of one-dimensional cuts through the potential surface and to what extent the intermode coupling needs to be explicitly taken into account. This last issue is of particular interest as it provides insight into when one can unravel spectra through a series of fully anharmonic, reduced-dimensional slices through the global potential surface. This will become particularly powerful as we consider larger ion–water complexes involving multiple water molecules and possibilities for proton translocation.^{24,25}

II. Experimental Details

The gas-phase, Ar solvated clusters were made by introducing trace amounts of the neutral precursor for the anions of interest ($CHCl_3$, CH_2Br_2 , and CH_3I for the Cl^- , Br^- , and I^- anions, respectively) and H_2O vapor through independently pulsed valves into the low-pressure side of a pulsed free-jet supersonic expansion of Ar gas. The mixed expansion was then ionized by a counterpropagating 1 keV electron beam and mass selected in a tandem time-of-flight photofragmentation spectrometer described previously in detail.^{26,27}

The infrared spectra were recorded by monitoring argon predissociative mass loss^{13,19}



The argon-solvated anionic clusters were photoexcited with pulses from a 10 Hz, Nd:YAG-pumped, OPO/OPA laser (LaserVision) continuously tuned from ~ 800 to 3800 cm^{-1} . The resolution of the laser is $\sim 3\text{ cm}^{-1}$. The spectra reported here result from the summation of between 15 and 30 individual scans and are normalized to the OPO/OPA output power. Line positions are accurate to 5 cm^{-1} as determined by monitoring the frequency of the 800 nm signal beam of the OPO with a wavemeter (Lambdameter LM-007).

III. Theoretical Details

The approach used to characterize the $X^- \cdot H_2O$ complexes is based on both ab initio electronic structure calculations and harmonic analyses. Ab initio calculations are also used to obtain one-dimensional slices of both the potential energy (PES) and dipole moment surfaces for the two vibrational modes of interest. These surfaces are then used to calculate vibrational energies, wave functions, and oscillator strengths in a basis of sine and cosine functions.

IIIA. Electronic Structure Calculations. All electronic structure calculations are performed using the GAUSSIAN 03²⁸ program package. One-dimensional potential energy and dipole moment surfaces are calculated using second-order Möller–Plesset perturbation theory (MP2) and large, diffuse Dunning basis sets (aug-cc-pVTZ). For the $I^- \cdot H_2O$ systems, a 28 electron core pseudopotential (PP) and corresponding basis set are used for iodine (aug-cc-pVTZ-PP).^{29,30} This core potential and basis set are chosen because the pseudopotential is parametrized for halogen–oxygen interactions as well as for anionic properties, and the basis set is of similar size and quality as that used for the lighter atoms. This combination of theory/basis has proven to be reliable for these hydrogen-bonded systems while at the same time remaining computationally feasible.³¹

Using this level of theory, we perform two sets of calculations. First, we evaluate the harmonic spectra at the minimum-energy geometries of the four isotopologues of each $X^- \cdot H_2O$

TABLE 1: Equilibrium Geometries of $X^- \cdot H_2O$ Complexes^a

parameter	$Cl^- \cdot H_2O$	$Br^- \cdot H_2O$	$I^- \cdot H_2O$
r_{OH_f}	0.961	0.961	0.961
r_{OH_b}	0.991	0.986	0.981
r_{XH_b}	2.115	2.292	2.548
$\phi_{H_fOH_b}$	100.7	100.6	100.7
ϕ_{OH_bX}	168.9	167.5	165.4
$\psi_{H_fOH_bX}$	180.0	180.0	180.0
$ \theta_{ip}^{C_s} $	47.62	47.96	48.52

^a All distances, r , have units of angstroms (Å), and all angles, ϕ , ψ , and θ , have units of degrees (°).

complex. We also evaluate the potential and dipole surfaces along two different one-dimensional slices through the global six-dimensional potentials, one along the ip bend coordinate and a second as a function of the oop bend coordinate.

The ip bend angle (θ_{ip}) is depicted in Figure 1C and is defined as the angle between one of the OH bonds and the OX^- axis. The ip bend angle is calculated in increments of 5.0° starting from the C_{2v} transition state, where the HOX^- angle is represented by $\theta_{HOX}^{C_{2v}}$. More specifically

$$\theta_{ip} = \begin{cases} \theta_{HOX}^{C_{2v}} - \theta_{H_1OX} & \theta_{ip} < 0 \\ \theta_{H_2OX} - \theta_{HOX}^{C_{2v}} & \theta_{ip} > 0 \end{cases} \quad \text{for} \quad (2)$$

where the C_{2v} structure is shown in Figure 1B. The values of θ_{ip} at the C_s minima depend on the equilibrium HOH angle in the complex and differ slightly among the halides. The equilibrium values for the three halides are reported in Table 1. For the calculations of the electronic energy as a function of this coordinate, the complex is constrained to remain planar. The OH_b , OH_f , and OX^- distances and the water angle are relaxed to their optimized values. It should be noted that since halide–water complexes have C_s symmetry in their equilibrium configurations, the one-dimensional PESs along the ip bend coordinate, $V(\theta_{ip})$, are symmetric about their C_{2v} geometries, and $\theta_{ip} = 0^\circ$ at this stationary point.

The other coordinate of interest is the oop bend angle (θ_{oop}), shown in Figure 1D. To obtain the potential as a function of the oop bend coordinate, we perform a scan in χ_{oop} , which is the angle between the plane that contains the water molecule and the plane defined by the heavy atom axis and the OH_f bond. It is varied over a range of 0.01 – 75.01° in increments of 5.0° in the calculated cuts through the potential along this coordinate. In these calculations of the electronic energy as a function of an oop bend angle (χ_{oop}), only the OH_b distance and the water angle are relaxed, while the OX^- distance, the OH_f bond length, and the H_fOX^- angle are constrained to their equilibrium values. Because the equilibrium structure is planar, the one-dimensional potentials evaluated as a function of χ_{oop} , $V(\chi_{oop})$, are symmetric about $\chi_{oop} = 0^\circ$.

The above treatment defines the oop bend angle as the angle between two planes, rather than the angle between the OH_b bond and the molecular plane (which we will make the ab plane). In order to obtain the latter description of the oop bend (θ_{oop}), we take advantage of the fact that the scans employed a dummy atom (Y) that is coplanar with the halide ion and the OH_f bond. The dummy atom has a YOX^- angle that is constrained in the scans. To determine θ_{oop} , we first define the a -axis to contain the two heavy atoms (O and X^-) and the dummy atom to lie in the ab plane. We then equate θ_{oop} with the angle between the OH_b bond and the ab plane. Although χ_{oop} and θ_{oop} are not

identical, their values differ by no more than 1° over the range of these coordinates for which the wave functions have amplitude.

The dipole surfaces, which are plotted in Supporting Information, are evaluated as functions of each of these coordinates and are obtained for the same values of θ_{ip} and θ_{oop} that are used to evaluate the corresponding potentials. In order to separate the three components of the dipole moment, we need to obtain a consistent definition of the three Cartesian axes. We start by shifting the origin of the molecule to the center of mass of the complex. For the ip bend, we use the Eckart conditions,³² as described by Louck and Galbraith.³³ For this treatment, we need to choose a reference geometry, and we use the C_{2v} saddle point structure, shown in Figure 1B. Since the definition of θ_{oop} relies on the definitions of the a , b , and c axes, we rotate the dipole moment vectors to this axis system.

The ranges for the one-dimensional potential and dipole moment surfaces are chosen such that they span the ranges sampled by the vibrational wave functions of the states of interest.

IIIB. Vibrational Coordinates and Hamiltonians. IIIBi. In-Plane (ip) Bend. The ip bend motion is strongly coupled to several other vibrational modes, particularly, the HOH bend. This coupling is illustrated by the plots of the value of the water angle as a function of θ_{ip} , shown in Figure 2A. Here, the water angle varies by $\sim 15^\circ$ for $0 \leq \theta_{ip} \leq 90^\circ$. While the two OH bond lengths also change along this cut, the differences between their values at the C_s minima and the C_{2v} saddle point are only 1–2%. Plots that show these effects are provided in the Supporting Information.

In order to include the effects of the couplings of the ip bend to the other coordinates, we employ a reaction path formalism.^{34,35} This approach allows us to incorporate the energies in the remaining degrees of freedom at the harmonic level and provides effective (i.e., vibrationally adiabatic) potential energy surfaces as a function of θ_{ip} . In this representation, the potential energy as a function of θ_{ip} can be expressed as

$$V(\theta_{ip}) = V_{MEP}(\theta_{ip}) + \sum_i^{3N-7} \left(n_i + \frac{1}{2} \right) \omega_i(\theta_{ip}) \quad (3)$$

where $V_{MEP}(\theta_{ip})$ is the potential energy along the minimum-energy path, or the energies calculated by the electronic structure methods listed above, and the ω_i are the harmonic frequencies of the $3N - 7$ degrees of freedom.^{34,35} The n_i provide the number of quanta in the remaining $3N - 7$ degrees of freedom in evaluating the potential.

The Hamiltonian for these one-dimensional calculations (in atomic units) is given by

$$\hat{H}_{ip} = -\frac{d}{d\theta_{ip}} b_{eff}(\theta_{ip}) \frac{d}{d\theta_{ip}} + V(\theta_{ip}) + V'(\theta_{ip}) \quad (4)$$

Transforming the kinetic energy operator from Cartesian to internal coordinates introduces a coordinate dependence to this operator and produces an additional term in the Hamiltonian, $V'(\theta_{ip})$. The effective mass term in eq 4, $b_{eff}(\theta_{ip})$, is derived from the G -matrix elements. The functional forms of the G -matrix elements and the additional $V'(\theta_{ip})$ terms used in the ip bend study are derived from the expressions given by Frederick and Woywod.³⁶ Because $X^- \cdot H_2O$ complexes have C_s symmetry, there are five modes with A' symmetry and one mode with A'' symmetry. Thus, the G -matrix is block diagonal with a 5×5 and a 1×1 block, where the 1×1 block constitutes the oop bend. The effective mass for the ip bend, $b_{eff}(\theta_{ip})$, contains contributions from the remaining terms in the 5×5 block due

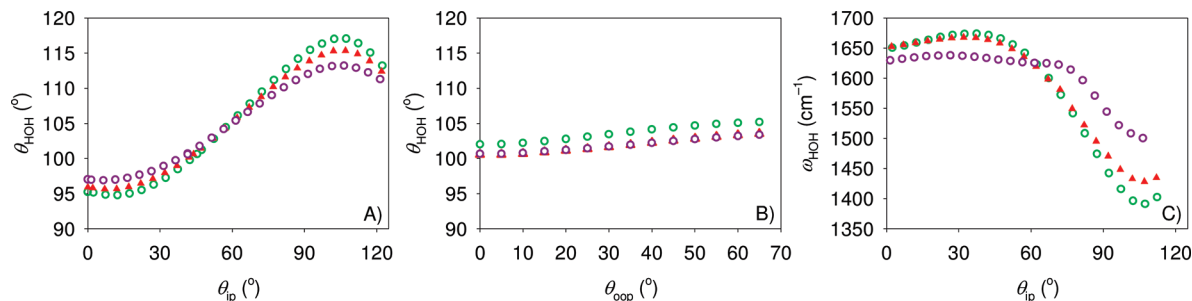


Figure 2. Plot of the water angle as a function of both (A) the ip bend angle (θ_{ip}) and (B) the oop bend angle (θ_{oop}). The water bend frequency is also plotted as a function of the ip bend angle in (C). $Cl^- \cdot H_2O$ is shown as the green circles, $Br^- \cdot H_2O$ as the red triangles, and $I^- \cdot H_2O$ as the purple circles.

to changes of the other symmetric coordinates along the reaction path.

It should be noted that partial deuteration will lower the symmetry of $b_{eff}(\theta_{ip})$, $V(\theta_{ip})$, and $V'(\theta_{ip})$ in eqs 3 and 4, as these terms depend on the mass of the two hydrogen atoms. The mass dependence of $V'(\theta_{ip})$ is reflected in its functional form.³⁶ The mass dependence of $V(\theta_{ip})$ is more subtle and is introduced through the mass dependence of the harmonic frequencies in eq 3. To reflect the asymmetry of the singly deuterated complexes, we define $\theta_{ip} > 0$ when X^- is closer to the deuterium atom ($X^- \cdot DOH$) and $\theta_{ip} < 0$ when X^- is closer to the hydrogen atom ($X^- \cdot HOD$).

IIIBii. Out-of-Plane (oop) Bend. On the basis of symmetry, the oop bend is much less strongly coupled to the other vibrational degrees of freedom. This is supported by the dependence of θ_{HOH} on θ_{oop} , plotted in Figure 2B. In contrast to its variations with θ_{ip} , the θ_{HOH} value changes by $< 4^\circ$ when θ_{oop} is increased from 0 to 70° . On the basis of this, we find that the reaction path approach described above is not necessary to describe the dependence of the potential surface on the oop bend angle, and we employ a simplified version of eq 4 for the oop bend

$$\hat{H}_{oop} = -\frac{d}{d\theta_{oop}} b_{eff}(\theta_{oop}) \frac{d}{d\theta_{oop}} + V_{MEP}(\theta_{oop}) \quad (5)$$

As in the calculation involving θ_{ip} , $V_{MEP}(\theta_{oop})$ is the one-dimensional PES for θ_{oop} and is obtained from the electronic structure calculations described above.

In the case of the oop bend, $V'(\theta_{oop}) = 0$ because of symmetry and therefore is not included in eq 5. The $b_{eff}(\theta_{oop})$ terms are the elements of the aforementioned 1×1 block of the G -matrix. These 1×1 elements are derived from the Wilson B -matrix³⁷ and are calculated using finite differencing.

IIIC. Numerical Details. In order to make a direct comparison with the experimental results, in addition to obtaining the transition frequencies, we calculate the relative line strengths

$$M_{i,n_i} = \frac{|\langle n_i | \vec{\mu} | 0 \rangle|^2}{|\langle n_{HOH} = 1 | \vec{\mu} | 0 \rangle|^2} \quad (6)$$

Here, n_i represents the number of quanta in the i th mode, and the calculated line strength for the water bend (in the denominator) is evaluated at the harmonic level. The line strengths for the four isotopologues of each $X^- \cdot H_2O$ complex are normalized independently.

The effective mass terms in eqs 4 and 5 are calculated at the same values of the angles as those used to determine the respective ab initio potential and dipole surfaces. All integrals are evaluated numerically, and the terms in eqs 4–6 that depend on the bend coordinates are interpolated using cubic splines.

This study is performed in a basis of cosine, $\cos(m\theta)$, and sine, $\sin(m'\theta)$, functions, where m and $m' \leq 100$.

IV. Appearance of the Spectra

In Figures 3–7, we present the argon predissociation spectra for the various halide ion–water complexes. The observed transition frequencies are collected in Table 2. For comparison, the harmonic frequencies and associated relative line strengths are reported in Table 3. We have chosen to organize these spectra first by halogen for the pure water and pure deuterium isotopologues (Figures 3–5) and then present a comparison of the mixed isotope data for three halogens in Figures 6 and 7. While the spectra reported in Figures 6 and 7 are identical, features assignable to the $X^- \cdot HOD$ isotopomers are highlighted in Figure 6, while those traced to $X^- \cdot DOH$ are highlighted in Figure 7.

The spectra for $Cl^- \cdot H_2O$ and $Cl^- \cdot D_2O$ are displayed in Figure 3. The fundamentals in the three intramolecular water modes (ν_{HOH} , ν_{OH_b} , ν_{OH_f}) are color-coded to follow the expected red shifts upon deuteration. Similar trends are found for the Br^- and I^- complexes, shown in Figures 4 and 5, respectively. In the case of the $Cl^- \cdot H_2O$ complex, we report a fourth fundamental, the oop bend (ν_{oop}), but this transition shifts out of our spectral detection range for the deuterated analogues. As is indicated in Table 3, the fundamentals in the remaining two modes are below 400 cm^{-1} , putting them outside of our detection range.

As we compare and contrast the spectra of the 12 species studied here, we will divide the spectra into three regions. We will start the discussion with the high-frequency region that includes the OH and OD stretch fundamentals. Next, we consider the low-frequency region that contains the fundamental in the oop bend. Finally, we consider the intermediate region that contains the water bend fundamental.

IVA. OH and OD stretch Fundamental Region [2250–3750 cm^{-1}]. As noted in earlier studies,^{14–16,23} the interaction of water with a halide ion red shifts the bonded OH stretch frequency (ν_{OH_b}), while the frequency of the free OH stretch (ν_{OH_f}) is relatively unaffected by the presence of the halide ion. The interaction with the halide ion also increases the intensity of the ν_{OH_b} band relative to the intensity of the fundamental in the free OH stretch. In going from chloride to iodide, the halide–water interaction strength decreases, and the position of ν_{OH_b} shifts to higher frequency, moving closer to the frequency of the ν_{OH_f} band. These trends are reproduced in the harmonic calculations in which the free OH/OD stretch frequencies change by less than 10 cm^{-1} for these complexes, while the ν_{OH_b} frequencies increase by 250 cm^{-1} from the chloride to the iodide complex. Similar trends are seen for the fully deuterated complexes.

TABLE 2: Experimentally Observed Transition Frequencies of the $X^- \cdot H_2O$ Complexes

species	observed transitions, cm^{-1}								
	ν_{oop}	$2\nu_{oop}$	ν_{HOH}	$\nu_{HOH} + \nu_{ip}$	ν_{OH_b}	$2\nu_{HOH}$	$\nu_{OH_b} + \nu_{OX}$	$2\nu_{HOH} + \nu_{OX}$	ν_{OH_t}
$Cl^- \cdot H_2O$	738	1404	1653	1962	3146	3289	3356	3521	3697
$Cl^- \cdot DOH$		1057	1404	1687	2357	2880	2547		3697 ^b
$Cl^- \cdot HOD$		1369	1507	1750	3156	2970/2990 ^a	3360		2716
$Cl^- \cdot D_2O$		1028	1219	1446	2341	2429	2541	2609	2737
$Br^- \cdot H_2O$	664 ^c	1262	1647	1870/1922 ^d	3296	3238	3461	3396	3695
$Br^- \cdot DOH$		959	1409	1638	2445				3688 ^e
$Br^- \cdot HOD$		1227	1484		3294	2950	3451		
$Br^- \cdot D_2O$			1216	1405	2451	2400			2726
$I^- \cdot H_2O$		1098	1639	1799/1890 ^d	3393/3422 ^a	3246	3524/3552 ^a	3367	3692/3706 ^a
$I^- \cdot DOH$		862	1417	1585	2526				3705 ^f
$I^- \cdot HOD$		1068	1464	1641	3407				
$I^- \cdot D_2O$			1208		2511/2527 ^a	2401			2728

^a Transition appears as a doublet in the experimental spectrum. ^b Value assigned based on suppression of the fine structure with multiple Ar attachment (ref 12). ^c Frequency from ref 15. ^d Value is the higher-energy component of a tunneling doublet. ^e Value assigned by taking the centroid of the rotational substructure. ^f Frequency from ref 20.

TABLE 3: Harmonic Fundamental Frequencies for $X^- \cdot H_2O$ Complexes with M_{i,j_i} Values (eq 6) Given in Parentheses

species	ν_{OH_t}	ν_{OH_b}	ν_{HOH}	ν_{ip}	ν_{OX}	ν_{oop}
$Cl^- \cdot H_2O$	3894 (0.1380)	3335 (5.7054)	1669 (1.0000)	366 (2.1619)	203 (2.2109)	754 (1.1876)
$Cl^- \cdot DOH$	3891 (0.0785)	2428 (3.8788)	1413 (1.0000)	311 (1.8074)	199 (2.0886)	549 (1.2322)
$Cl^- \cdot HOD$	2825 (0.0833)	3341 (8.4162)	1516 (1.0000)	298 (2.0268)	198 (3.7648)	751 (1.4779)
$Cl^- \cdot D_2O$	2834 (0.2528)	2422 (6.4806)	1219 (1.0000)	265 (2.0174)	195 (4.1773)	545 (1.6452)
$Br^- \cdot H_2O$	3889 (0.1570)	3426 (4.4919)	1664 (1.0000)	339 (2.1525)	170 (0.8422)	704 (1.0631)
$Br^- \cdot DOH$	3885 (0.0828)	2494 (3.0323)	1417 (1.0000)	286 (1.7134)	166 (0.7754)	515 (1.1137)
$Br^- \cdot HOD$	2821 (0.0748)	3432 (6.7951)	1503 (1.0000)	277 (2.2353)	165 (1.5393)	700 (1.2989)
$Br^- \cdot D_2O$	2830 (0.2770)	2487 (4.9930)	1216 (1.0000)	245 (2.1082)	161 (1.6264)	509 (1.4067)
$I^- \cdot H_2O$	3896 (0.1593)	3608 (2.6117)	1635 (1.0000)	346 (1.8600)	137 (0.4506)	632 (0.8899)
$I^- \cdot DOH$	3895 (0.1076)	2620 (1.7201)	1408 (1.0000)	289 (1.3683)	134 (0.4129)	466 (0.9448)
$I^- \cdot HOD$	2831 (0.1035)	3609 (4.0699)	1462 (1.0000)	288 (2.1012)	131 (0.8270)	627 (1.0602)
$I^- \cdot D_2O$	2836 (0.2888)	2614 (2.7475)	1195 (1.0000)	253 (1.7740)	128 (0.8271)	458 (1.1185)

In the case of the partially deuterated complexes (shown in Figures 6 and 7), the bonded OH or OD fundamental dominates in all of the $X^- \cdot HDO$ mixed isotopomers. The frequency of the ν_{OH_b} band is found to be within 20 cm^{-1} of the band in the corresponding H_2O or D_2O complexes. In the complexes for which the free OH or OD stretch is assigned, the frequencies

of the free hydrogen stretches are within 20 cm^{-1} of the corresponding H_2O or D_2O complexes.

Several other bands have been previously assigned that are close in energy to the OH_b and OD_b stretch fundamentals. In particular, the first overtone in the HOH bend is close in frequency to the fundamental band of the bonded OH stretch. There is a well-known Fermi resonance between the overtone in the water bend and the fundamental in the OH stretch of the same symmetry that typically occurs with an interaction matrix element on the order of 30 cm^{-1} .²² The magnitude of the red shift of the ν_{OH_b} fundamental depends on which halide is present. In the case of the bromide complexes with H_2O and D_2O , the red shift of the ν_{OH_b} band puts it within 60 cm^{-1} of the overtone in the water bend. In the iodide complexes, the bend overtone is to the red of the ν_{OH_b} fundamental, while it is found to the blue of the ν_{OH_b} fundamental in the chloride complexes. The smaller energy gap between the ν_{OH_b} and $2\nu_{HOH}$ bands in the bromide complexes leads to larger mixing of these two states, as is evidenced by the relative intensity of the two bands, plotted in turquoise and red. In the spectra for $Br^- \cdot H_2O$ and $Br^- \cdot D_2O$, the ν_{OH_b} and $2\nu_{HOH}$ bands have intensities that differ by less than a factor of 2 (as seen in Figure 4), while the intensity of the bend overtone is much lower than the OH stretch fundamental in the Cl^- and I^- spectra reported in Figures 3 and 5, respectively.

The bend frequency in HOD is intermediate between that of H_2O and D_2O . As is seen in Figure 6, the overtone in the HOD

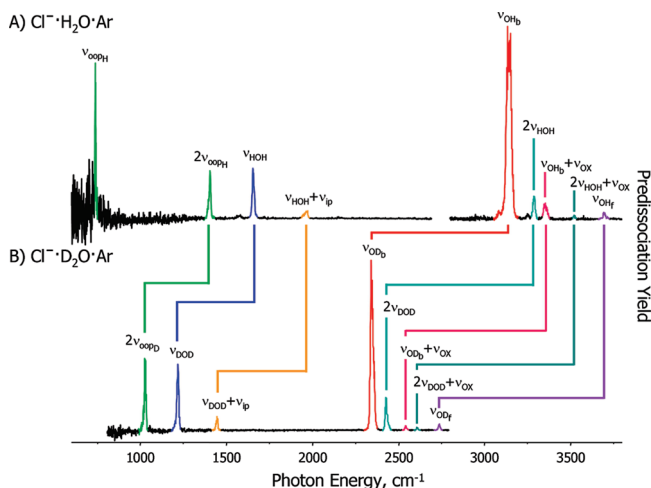


Figure 3. The vibrational predissociation spectra of (A) $Cl^- \cdot H_2O \cdot Ar$ and (B) $Cl^- \cdot D_2O \cdot Ar$. The shifts in absorption frequencies upon isotopic substitution of the hydrogen atoms are indicated.

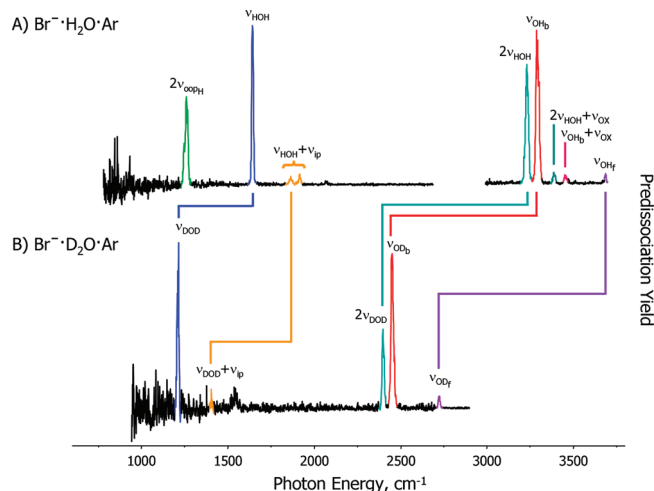


Figure 4. Same as Figure 3 but for (A) $Br^- \cdot H_2O \cdot Ar$ and (B) $Br^- \cdot D_2O \cdot Ar$.

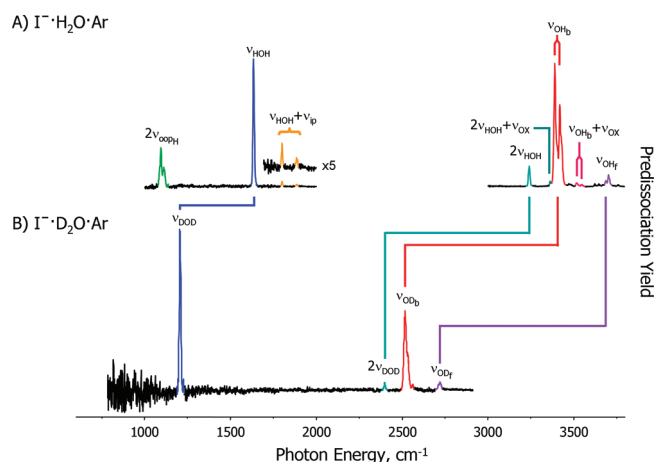


Figure 5. Same as Figure 3 but for (A) $I^- \cdot H_2O \cdot Ar$ and (B) $I^- \cdot D_2O \cdot Ar$.

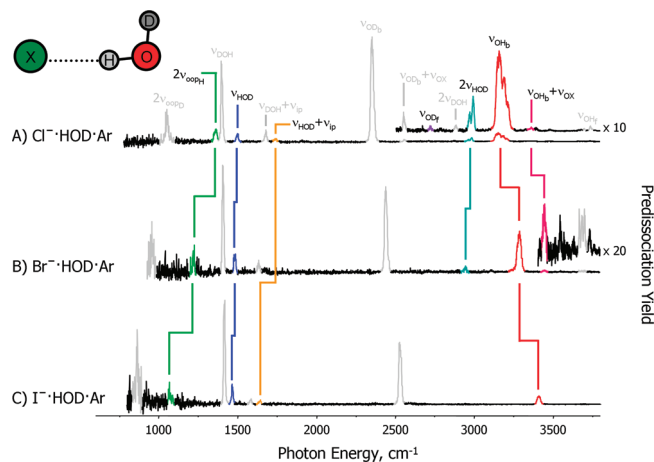


Figure 6. The vibrational predissociation spectra of (A) $Cl^- \cdot HOD \cdot Ar$, (B) $Br^- \cdot HOD \cdot Ar$, and (C) $I^- \cdot HOD \cdot Ar$. The frequency shifts upon X^- substitution are revealed as well as the differences in frequencies due to H versus D in the bound position.

bend is now to the red of the fundamental in the bonded OH stretch in the $Cl^- \cdot HOD$ complex. With the shift of the ν_{OH_b} fundamental to higher frequency in the bromide and iodide complexes, the intensity of the $2\nu_{HOD}$ band is much smaller in the $Br^- \cdot HOD$ complex, and the corresponding band is not evident in the spectrum for the $I^- \cdot HOD$ complex.

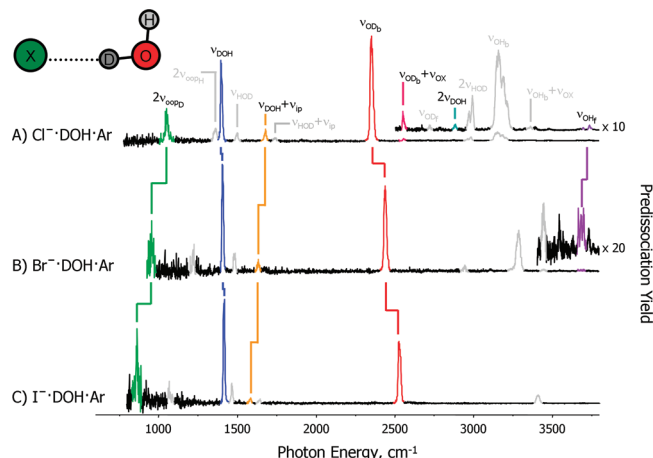


Figure 7. Same as Figure 6 but for (A) $Cl^- \cdot DOH \cdot Ar$, (B) $Br^- \cdot DOH \cdot Ar$, and (C) $I^- \cdot DOH \cdot Ar$.

There is another, lower-intensity band, which is found to the blue of the ν_{OH_b} transition in the $Cl^- \cdot H_2O$, $Cl^- \cdot D_2O$, $Br^- \cdot H_2O$, and $I^- \cdot H_2O$ spectra. This has been assigned to the $\nu_{OH_b} + \nu_{OX}$ combination band.¹⁵ This assignment is based on the evolution of its shift relative to ν_{OH_b} over the series and the fact that higher-dimensional studies of other similar species (specifically, $Cl^- \cdot H_2O$, $F^- \cdot H_2O$, $H_4O_2^+$, and $H_5O_2^+$)^{14,38–41} have shown evidence for strong coupling between ν_{OH_b} and the heavy atom stretch, which involves the two atoms that the shared hydrogen atom is vibrating between. In $Br^- \cdot H_2O$, there is an additional peak between ν_{OH_b} and $\nu_{OH_b} + \nu_{OX}$. On the basis of the strong Fermi resonance in this complex, this band is assigned to the $2\nu_{OH_b} + \nu_{OX}$ combination band. These combination bands also appear in the $Cl^- \cdot H_2O$ and $Cl^- \cdot D_2O$ spectra (Figure 3). However, they are displaced to the blue of the $\nu_{OH_b} + \nu_{OX}$ feature as the ion-bound OH stretch falls to the red of the bend overtone. Fine structure is also observed on the ν_{OH_b} fundamentals of the $I^- \cdot H_2O$ and $Cl^- \cdot HOD$ complexes (Figures 5A and 6A). We have reported the evolution of these features in both the $I^- \cdot H_2O$ and $Cl^- \cdot H_2O$ complexes with increasing numbers of Ar atoms in two previous studies^{12,13} and find that, in both cases, the structure is highly dependent on the extent of Ar solvation. In the chloride case, this effect was traced to the different isomers available until a sharp band evolved as the icosahedral solvation shell was filled with 11 Ar atoms.¹² The analogous doublet structure in the $I^- \cdot H_2O$ complex was also explored here and found to persist upon attachment of at least 7 Ar atoms; as such, it appears to arise from an intrinsic coupling in the hydrate rather than an effect due to solvation.

IVB. Out-of-Plane Bend Fundamental Region [below 1000 cm^{-1}]. In the low-frequency region of the $Cl^- \cdot H_2O$ spectrum, the band at 738 cm^{-1} is observed and has been identified as the fundamental in the oop bend.¹⁵ This frequency is well-reproduced by our one-dimensional calculations, reported in Table 4, as well as by six-dimensional calculations previously reported by Rheinecker and Bowman.^{41,42} Analogous features are not seen in any of the other spectra reported in Figures 3–7. This is consistent with the harmonic frequencies, which anticipate this band to red shift for the heavier halides. Furthermore, its harmonic frequencies in the $X^- \cdot H_2O$ and $X^- \cdot HOD$ complexes differ by less than 5 cm^{-1} . Likewise the harmonic frequencies of the oop bend in $X^- \cdot D_2O$ and $X^- \cdot DOH$ are nearly identical. Since the fundamental transitions are at the edge or slightly below the experimental detection range, experimental verification of this will require identification of overtone or combination bands involving this mode.

TABLE 4: Calculated Fundamental and Overtone Transition Frequencies for the In-Plane, Water, and Out-of-Plane Bends (given in cm^{-1})

species	ip bend					HOH bend		oop bend	
	$n_{\text{HOH}} = 0^a$		6-d ^b	$n_{\text{HOH}} = 1^c$		1-d ^d	6-d ^b	1-d ^e	6-d ^b
$\text{Cl}^- \cdot \text{H}_2\text{O}$	333/334 577/577	343/344 666/666	362	1985/1985	1993/1994	1661	1660	721 (0.8697) 1412 (0.3747)	715 1409
$\text{Cl}^- \cdot \text{DOH}$	291 539		319.3	1698		1408	1414.0	531 (0.6893) 1046 (0.1969)	540.1 1064
$\text{Cl}^- \cdot \text{HOD}$	280 523		305.1	1772		1507	1523.2	721 (1.2477) 1412 (0.5392)	724.9 1423
$\text{Cl}^- \cdot \text{D}_2\text{O}$	249/249 467/467	249/249 478/478	264.4	1459/1459	1459/1459	1215	1221.8	531 (1.1427) 1046 (0.3281)	526.1 1041
$\text{Br}^- \cdot \text{H}_2\text{O}$	286/287 495/496	310/311 613/614		1936/1937	1958/1959	1656		669 (0.6922) 1309 (0.3512)	
$\text{Br}^- \cdot \text{DOH}$	259 463			1672		1411		493 (0.5012) 970 (0.1779)	
$\text{Br}^- \cdot \text{HOD}$	247 461			1728		1495		669 (1.0113) 1309 (0.5135)	
$\text{Br}^- \cdot \text{D}_2\text{O}$	221/221 396/396	223/223 426/426		1429/1429	1431/1431	1211		493 (0.8290) 970 (0.2946)	
$\text{I}^- \cdot \text{H}_2\text{O}$	185/189 399/404	258/263 543/548		1817/1822	1891/1895	1633		596 (0.5336) 1163 (0.3246)	
$\text{I}^- \cdot \text{DOH}$	195 357			1609		1407		440 (0.3613) 864 (0.1580)	
$\text{I}^- \cdot \text{HOD}$	181 384			1624		1459		596 (0.7972) 1163 (0.4852)	
$\text{I}^- \cdot \text{D}_2\text{O}$	160/161 277/278	178/179 353/354		1355/1355	1373/1373	1194		440 (0.5886) 864 (0.2575)	

^a For each isotopic species, two sets of frequencies are given, the frequency of the fundamental transition (first row) and the frequency of the overtone transition (second row). As is discussed in the text for $\text{X}^- \cdot \text{H}_2\text{O}$ and $\text{X}^- \cdot \text{D}_2\text{O}$, the two columns represent transitions for the two members of the tunneling doublets. For more details, see Table 5. ^b Full six-dimensional calculations from ref 41. ^c Frequencies for the combination band of $\nu_{\text{HOH}} + \nu_{\text{ip}}$. As is discussed in the text for $\text{X}^- \cdot \text{H}_2\text{O}$ and $\text{X}^- \cdot \text{D}_2\text{O}$, the two columns represent transitions for the two members of the tunneling doublets. ^d Water bend frequencies are the differences in the zero-point levels obtained from eq 4 for $n_{\text{HOH}} = 0$ and 1. ^e Numbers in parentheses represent the line strengths of the oop bend transition obtained from eq 6.

TABLE 5: In-Plane Bend Fundamental and Overtone Frequencies (in cm^{-1}) and Line Strengths (in Debye²) for the Isotopologues of $\text{Cl}^- \cdot \text{H}_2\text{O}$

species	transition	frequency	<i>a</i> -type ^a	<i>b</i> -type ^a	$M_{\text{ip},n_{\text{ip}}}^b$
$\text{Cl}^- \cdot \text{H}_2\text{O}$	1 \leftarrow 0	333	0.02790	0.03038	2.43854
	1 \leftarrow 0	343	0.02980	0.02753	2.39880
	2 \leftarrow 0	577	0.00600	0.00004	0.25272
	2 \leftarrow 0	666	0.00494	0.00036	0.22148
$\text{Cl}^- \cdot \text{DOH}$	1 \leftarrow 0	291	0.02454	0.02460	1.91412
	2 \leftarrow 0	539	0.00329	0.00013	0.13341
$\text{Cl}^- \cdot \text{HOD}$	1 \leftarrow 0	280	0.02935	0.02368	3.19501
	2 \leftarrow 0	523	0.00340	0.00016	0.21445
$\text{Cl}^- \cdot \text{D}_2\text{O}$	1 \leftarrow 0	249	0.02542	0.02158	3.05589
	1 \leftarrow 0	249	0.02553	0.02145	3.05418
	2 \leftarrow 0	467	0.00278	0.00015	0.19040
	2 \leftarrow 0	478	0.00281	0.00019	0.19518

^a Transitions of *a*- and *b*-type differ in energy by the tunneling splitting of the ground state for $\text{Cl}^- \cdot \text{H}_2\text{O}$ and $\text{Cl}^- \cdot \text{D}_2\text{O}$, which is 0.2339 and 0.0068 cm^{-1} , respectively. The zero-point energies for $\text{Cl}^- \cdot \text{H}_2\text{O}$, $\text{Cl}^- \cdot \text{DOH}$, $\text{Cl}^- \cdot \text{HOD}$, and $\text{Cl}^- \cdot \text{D}_2\text{O}$ are 180, 152, 232, and 129 cm^{-1} , respectively. ^b The $M_{\text{ip},n_{\text{ip}}}$ values are obtained by summing the *a*- and *b*-type line strengths and normalizing with respect to the water bend transition for each isotopologue as shown in eq 6.

IVC. Water Bend Fundamental Region [1000 – 2250 cm^{-1}]. **IVCi. Water Bend Fundamental.** Next, we turn to the intermediate region (~ 1000 – 2000 cm^{-1}) of the spectra. A prominent feature that is seen in all of the spectra reported in

Figures 3–7 is the fundamental in the water bend, highlighted in dark blue. This feature occurs near 1650 cm^{-1} for the $\text{X}^- \cdot \text{H}_2\text{O}$ complexes and around 1200 cm^{-1} for the $\text{X}^- \cdot \text{D}_2\text{O}$ complexes and remains relatively unchanged with only a small red shift from chloride to iodide. The energies of the bend peaks are also in good agreement with the bare water bend frequencies, 1595 and 1178 cm^{-1} for the H_2O and D_2O species, respectively.⁴³ The water bend overtone, discussed above, is also hardly perturbed in the six $\text{X}^- \cdot \text{H}_2\text{O}$ and $\text{X}^- \cdot \text{D}_2\text{O}$ complexes. This serves to highlight the robustness of the water bend fundamental to halide substitution.

These trends are also seen in the harmonic frequencies, reported in Table 3, and in the frequencies obtained by taking the differences between the solutions to the Hamiltonian described by eqs 3 and 4 when $n_{\text{HOH}} = 1$ and 0, reported in Table 4. The frequency differences between the experimental and calculated values reported in Tables 2 and 4 are all smaller than 15 cm^{-1} , and much of this difference should be attributed to the failure of harmonic frequencies to capture anharmonic vibrations.

In Table 4, we also compare the present calculated frequencies for the chloride–water complexes to the frequencies reported by Rheinecker and Bowman,⁴¹ which are based on six-dimensional calculations. As the water bend is rather harmonic, the frequencies calculated by the reduced-dimensional approach used in the present calculations are in good agreement with those obtained from the six-dimensional calculations for all four isotopologues.

Before we move to other bands, it is interesting to note that in the singly deuterated species, the HOD bend frequencies differ

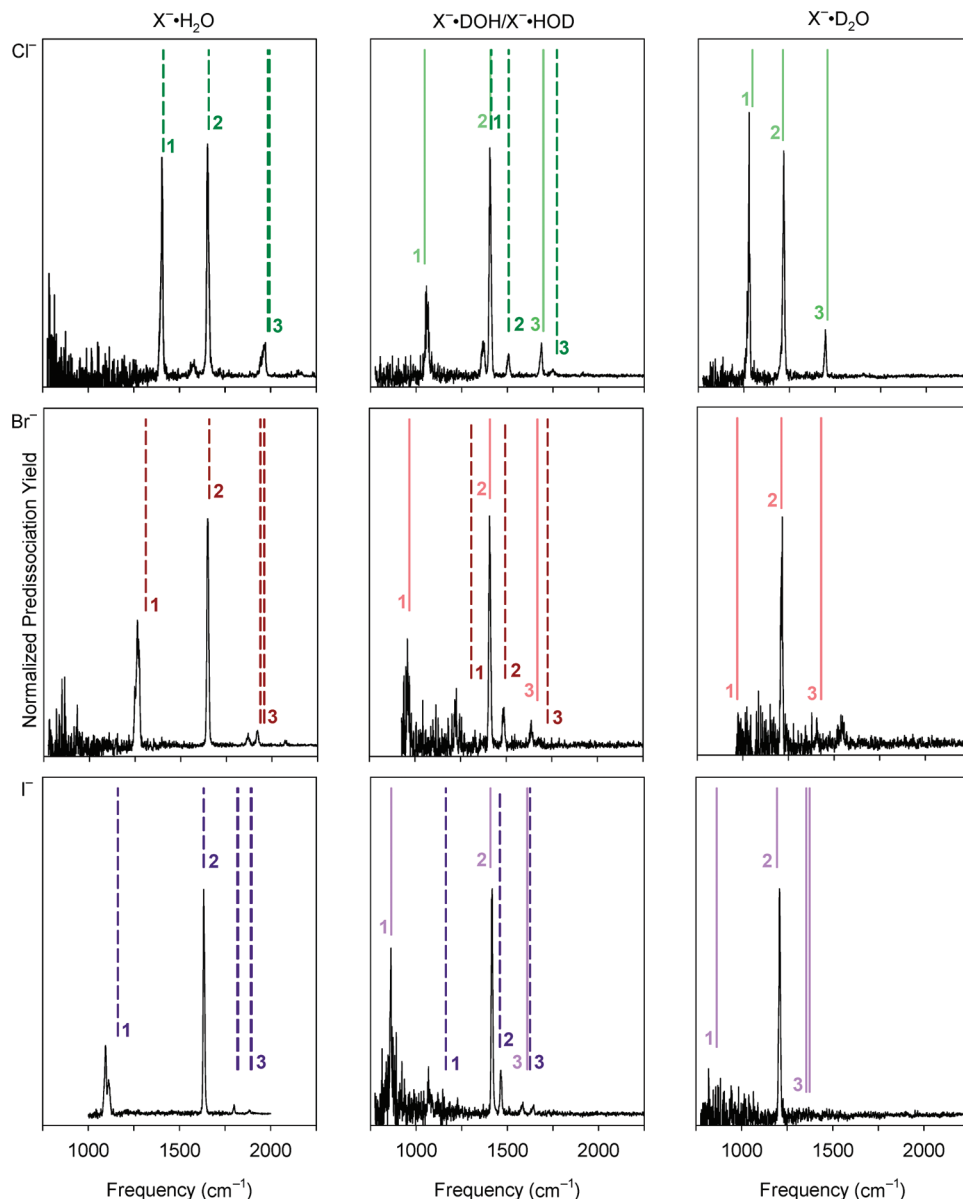


Figure 8. Comparison of calculated and experimental transition frequencies in the Ar predissociation spectra for $X^- \cdot H_2O$ (same as those shown in Figures 3–7). The calculated frequencies are shown as the sticks and are labeled as 1 for $2\nu_{oop}$, as 2 for ν_{HOH} , and as 3 for $\nu_{HOH} + \nu_{ip}$ (see Table 4 for $\nu_{HOH} + \nu_{ip}$ splittings). The solid lines refer to the $X^- \cdot DOH$ isomer and the dashed lines to the $X^- \cdot HOD$ isomer.

by as much as 100 cm^{-1} for the $X^- \cdot HOD$ and $X^- \cdot DOH$ complexes. In all cases, the average of these frequencies is close to the bare HOD bend frequency (1402 cm^{-1}).⁴⁴ The splitting of the frequency of the HOD bend in $X^- \cdot HOD$ and $X^- \cdot DOH$ and the observation that the bend frequency in the $X^- \cdot HOD$ complex is the larger of the two reflect the fact that the bending motions of these species involve larger displacements of the OH_b bond than those of the OH_f one. As a result, the so-called water bend has a contribution from rotation of the water molecule about an axis perpendicular to the molecular plane (e.g., ip bend character). This result hints to the fact that there is strong mixing of the two modes that are nominally pure water bend and pure ip bend motions.

IVCii. Overtone in the oop Bend. Of greater interest to the present work are the overtone and combination band structure that aid in the assignment of the low-energy modes. As indicated above, only in $Cl^- \cdot H_2O$ is the fundamental of ν_{oop} visible in the spectra reported in Figures 3–7. We must therefore rely on the overtone to assign these bands in the remaining species of the series. The first overtone for the oop bend of $Cl^- \cdot D_2O$

falls at 1028 cm^{-1} , leading to an assignment of $\sim 514\text{ cm}^{-1}$ for this fundamental. Similar treatments give values of ~ 631 and $\sim 549\text{ cm}^{-1}$ for $Br^- \cdot H_2O$ and $I^- \cdot H_2O$, respectively. These values for the ν_{oop} fundamentals must necessarily be approximate as anharmonicities would cause some shift in the true values. This can be seen in the locations of the $Cl^- \cdot H_2O$ and $Br^- \cdot H_2O$ transitions (Table 2), where the fundamental has been assigned (Br^- from ref 15). In the case of $I^- \cdot D_2O$, the first overtone of the oop bend disappears into the noise at the low-energy end of our laser, making assignment impossible.

The calculated anharmonic frequencies for these ν_{oop} -based transitions are reported in Table 4. In Figure 8, we overlay the calculated frequencies of the oop bend transitions (labeled as 1) onto the corresponding experimental spectra. This figure contains the same experimental spectra that are reported in Figures 3–7 and are scaled so that the height of the ν_{HOH} , ν_{DOH} , or ν_{DOD} band is the same in all of the plots. The calculated frequencies are shown with dashed lines for systems in which there is a bonded hydrogen atom, and the transitions in systems with a bonded deuterium atom are shown with solid lines.

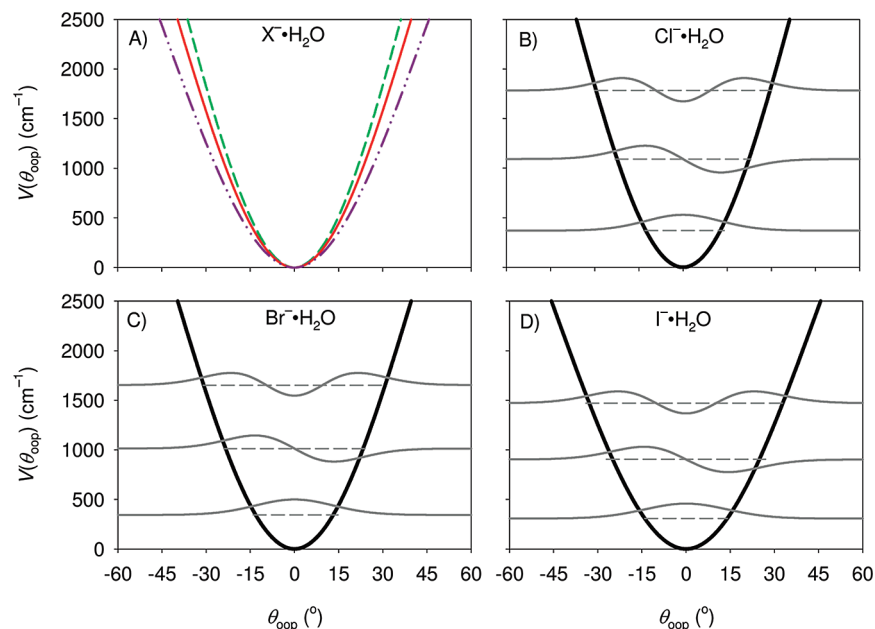


Figure 9. (A) One-dimensional cuts through the full-dimensional potentials as a function of the oop bend coordinate for $\text{Cl}^- \cdot \text{H}_2\text{O}$ (green dashed), $\text{Br}^- \cdot \text{H}_2\text{O}$ (red solid), and $\text{I}^- \cdot \text{H}_2\text{O}$ (purple dot-dashed). The oop bend wave functions (gray solid), energy levels (gray dashed), and potential surfaces (black) are also shown for (B) $\text{Cl}^- \cdot \text{H}_2\text{O}$, (C) $\text{Br}^- \cdot \text{H}_2\text{O}$, and (D) $\text{I}^- \cdot \text{H}_2\text{O}$.

Agreement between calculated and experimental transition frequencies for the overtone in the oop bend for the H_2O and D_2O complexes is good, with many of the differences being smaller than 20 cm^{-1} . Others are as large as 95 cm^{-1} ; however, in all cases, the largest differences between experiment and calculation are found for the $\text{X}^- \cdot \text{HOD}$ complexes. These differences likely reflect both limitations of reduced-dimensional treatments and the fact that, in the experiment, the species that is probed has been complexed with an argon atom. Moreover, if we compare the calculated frequencies for $\text{Cl}^- \cdot \text{H}_2\text{O}$ and $\text{Cl}^- \cdot \text{D}_2\text{O}$ to those obtained from six-dimensional calculations,³⁹ the differences are less than 6 cm^{-1} and under 20 cm^{-1} for $\text{Cl}^- \cdot \text{HOD}$ and $\text{Cl}^- \cdot \text{DOH}$.

We find that the frequency of the overtone in the oop bend decreases as the strength of the intermolecular interaction decreases. Given the robustness of the water bend frequencies, the red shift of the oop bend frequencies for the different halides may at first be surprising. To understand the origins of this shift, we turn to plots of the one-dimensional potentials as functions of θ_{oop} , shown in Figure 9A. Here, the width of these potentials increases from chloride to iodide. This change reflects the decrease in the strength and directionality of the $\text{X}^- \cdot \text{H}_2\text{O}$ interaction and illustrates an additional manifestation of the weakening of the halide–water bond seen in the red shift of ν_{OH_b} compared to the OH stretch in bare water, described above.

An interesting feature of the $2\nu_{\text{oop}}$ band is that its intensity is comparable to, and in some cases even larger than, the fundamental in the water bend. This feature of the spectra should be surprising for two reasons. First, at the harmonic level, the oop bend fundamental has an intensity that is no more than 1.65 times that of the water bend fundamental, and one generally expects the intensity of the overtone to be at least an order of magnitude smaller than that of the fundamental. Further complicating the situation, the components of the dipole moment that are responsible for the intensity of the fundamental and overtone in the oop bend are different, with the fundamental being a perpendicular transition whereas the overtone results from changes of the dipole moment components that lie in the molecular plane. The calculated intensities of the overtone,

reported in Table 4, also show larger intensities for the overtone than one might initially anticipate, although not as large as those observed in the experiment.¹⁵

Another unexpected aspect of the $2\nu_{\text{oop}}$ bands is the observation that the relative intensities of these overtones are similar for all of the halides, while the frequency spacing between the ν_{HOH} and $2\nu_{\text{oop}}$ bands increases as one increases the atomic number of the halide ion. This is seen most clearly in Figures 6 and 7, where we plot the spectra for $\text{X}^- \cdot \text{HOD}$ and $\text{X}^- \cdot \text{DOH}$ for all three halides, although it also holds for the $\text{X}^- \cdot \text{H}_2\text{O}$ and $\text{X}^- \cdot \text{D}_2\text{O}$ spectra reported in Figures 3–5. The robustness of this feature for all 12 spectra, thus, is not consistent with the large intensity of $2\nu_{\text{oop}}$ coming solely from intensity borrowing from the fundamental in the water bend. Rather, we suggested that it reflects a “charge sloshing” (vibrationally mediated intracomplex charge-transfer) mechanism, which has been discussed by Roscioli et al.¹⁵

To further explore the possible role of this effect on the spectra of the ip vibrational manifold, we review how this mechanism was handled theoretically in our analysis of the oop bend vibrational spectra. Two obvious sources of overtone intensity are mechanical anharmonicity and electrical anharmonicity. To evaluate their relative contributions, we model the dipole moment surface using a fixed charge approximation. Changes between the intensity that is predicted by this model and the one obtained using the full dipole surface provide insights into the magnitude of the contribution of electrical anharmonicity to the intensities of these transitions.

In the fixed charge approximation, we evaluate the intensities using static point charges on each of the four atoms in the complex. Here, the equilibrium atomic charges are obtained from a NBO^{45,46} analysis. (The dipole surfaces resulting from the fixed charge model are plotted in the Supporting Information.) When the $\text{Cl}^- \cdot \text{H}_2\text{O}$ coordinate-dependent dipole surface is used, we obtain an intensity ratio of the ν_{oop} overtone to the fundamental transition of 0.43 when a hydrogen is in the H_b position and a ratio of 0.29 for a deuterium in the H_b position. These ratios drop to 0.02 and 0.01, respectively, when the fixed charge model is used. Similar results are obtained for $\text{Br}^- \cdot \text{H}_2\text{O}$ and $\text{I}^- \cdot \text{H}_2\text{O}$

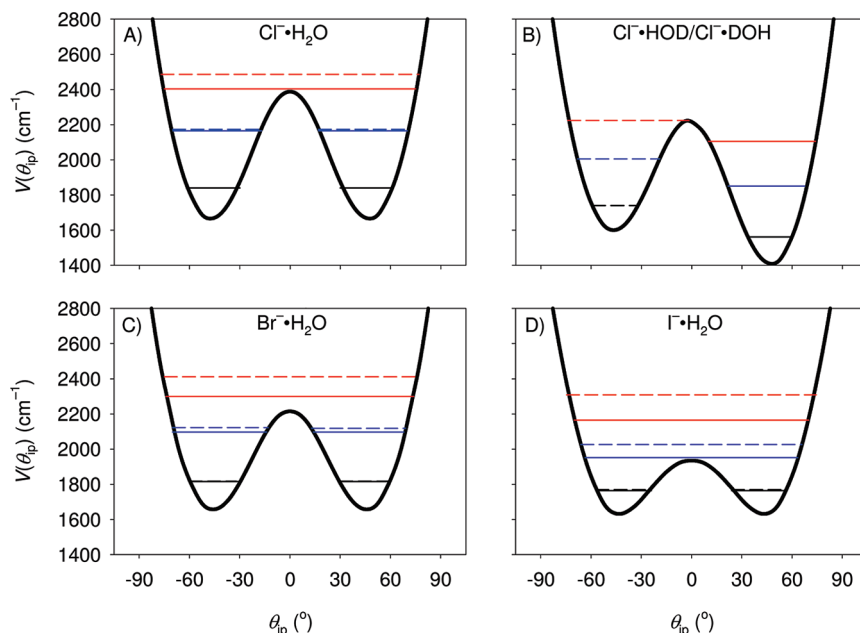


Figure 10. The ip bend potentials (thick black curves) and energy levels (horizontal lines) when one quantum of excitation in the water bend is included. In (A), (C), and (D), the energy levels are depicted with solid lines for symmetric states and dashed lines for states that have a node at $\theta_{ip} = 0^\circ$. For the HOD/DOH complex, solid lines are used to depict states that are localized in the $Cl^- \cdot DOH$ well, while dashed lines are used for states that are localized in the $Cl^- \cdot HOD$ well. In all cases, the ground states are depicted with black lines, and the states with one and two quanta in the ip bend are shown with blue and red lines, respectively.

and are reported in the Supporting Information. We have performed this analysis using Mulliken charges as well as setting the charges on the hydrogen atoms equal to +1, the halide to −1, and the oxygen to −2. In all three cases, the fixed charge model gave roughly the same ratio for the intensity of the overtone to the fundamental transition and did not reproduce the experimental intensity of the overtone.

This result is not surprising when one considers that the oop bending motion results in a charge redistribution among the four atoms. As discussed by Roscioli et al., when Mulliken charges were examined on the four atoms in $Cl^- \cdot H_2O$ as a function of the oop bend angle, we found that as the angle was increased from 0 to 90° , there was substantial charge rearrangement. Physically, this occurs because the out-of-plane displacement effectively “breaks” the highly directional hydrogen bond. Specifically, the charge on the halide tends toward −1, while the charges on the oxygen and hydrogen atoms approach their values in an isolated water molecule, calculated at the same level of theory.

IVCiii. In-Plane (ip) Bend. Next, we turn to signatures of ip bend excitation in the recorded spectra. Because of the double well character of the $X^- \cdot H_2O$ ip bend potentials, its fundamental band is anticipated to be more structured than the other fundamentals. In the ground vibrational state, the pairs of levels in $X^- \cdot H_2O$ and $X^- \cdot D_2O$ are nearly degenerate, with tunneling splittings ranging from 0.007 cm^{-1} in $Cl^- \cdot D_2O$ to 4.766 cm^{-1} in $I^- \cdot H_2O$. This range reflects the fact that the barrier to isomerization along the ip bend coordinate decreases as the polarizability of the anion increases. Likewise, the zero-point energy will decrease upon deuteration. The splitting is larger when there is one quantum in the ip bend, as is seen in panels A, C, and D of Figure 10. In the case of $I^- \cdot H_2O$, this pair of levels is above the isomerization barrier, and they differ in energy by 74 cm^{-1} , while the splittings for $Br^- \cdot H_2O$ and $Cl^- \cdot H_2O$ are 22 and 9 cm^{-1} , respectively. This double well character of the potential leads to the fundamental transitions appearing as two sets of doublets. As the splittings of the

ground-state levels are smaller than 5 cm^{-1} , at the resolution of the experiment, only doublets are expected to be resolvable. Their splitting reflects the energy gap between the excited state levels.

The frequencies and relative intensities of the resolvable bands (normalized to the fundamental in the water bend) are reported in Table 5 for the chloride complexes and in the Supporting Information for the other species. In the case of the chloride complexes, we can compare the fundamental frequencies to those reported by Rheinecker and Bowman.⁴¹ In general, the agreement is quite good; differences range from 15 to 30 cm^{-1} .

Interestingly, the higher dimensional calculations do not capture the tunneling splitting of the first excited states in the ip bend in either $Cl^- \cdot H_2O$ or in $Cl^- \cdot D_2O$. We suspect that this is a reflection of the fact that in their calculation, Rheinecker and Bowman used normal-mode coordinates evaluated at one of the two equivalent potential minima and employed a four-mode representation of the coupling.⁴¹ These choices must have artificially removed the equivalence of the two minima in their calculations, which would lead to the loss of the tunneling doublet structure in their calculated spectra.

As indicated above, the ip bend fundamental band in the $X^- \cdot H_2O$ and $X^- \cdot D_2O$ spectra is made up of four vibrational transitions. Two are *a*-type and go from the lower or upper member of the tunneling doublet with $n_{ip} = 0$ to the corresponding member of the tunneling doublet with $n_{ip} = 1$. There are also two *b*-type transitions that connect the other two pairs of states. As indicated by the results reported in Table 5, the two types of transitions have roughly equal intensity in the chloride complexes. As the splitting between the two states with $n_{ip} = 0$ is less than 0.25 cm^{-1} , the two bands will be overlapping. On the other hand, the 10 cm^{-1} splitting when $n_{ip} = 1$ in $Cl^- \cdot H_2O$ would lead to a pair of transitions spaced by 10 cm^{-1} that collapses to 0.5 cm^{-1} in $Cl^- \cdot D_2O$. Similar behavior is predicted for the iodide and bromide complexes. The decomposition of these bands is given in the Supporting Information.

In light of the large intensity in the overtone in the oop bend in these systems, we also calculated the frequencies and intensities for the ip bend transitions to the first overtone for each of these species using the MP2/aug-cc-pVTZ dipole surfaces. As is shown in Figure 10, in all cases, the fifth and sixth lowest-energy states (which correspond to two quanta in a localized ip bend vibration and are represented by the red lines) lie above the isomerization barrier in the $X^- \cdot H_2O$ complexes. For the $X^- \cdot D_2O$ species, these two states are above the barrier for the iodide complex and below the barrier for $Br^- \cdot D_2O$ and $Cl^- \cdot D_2O$. When we calculate the overtone intensities, we find that they are roughly an order of magnitude smaller than those for the fundamental. In addition, unlike the fundamental, where the *a*- and *b*-type transitions have roughly equal intensity, the intensities of the *a*-type transitions are between a factor of 10 and 100 larger than the intensity of the *b*-type transitions that comprise the $2\nu_{ip}$ bands.

When the fixed charge model, described above, is used to model the dipole moments for the ip bend, we find that the intensities decrease by a larger factor (10–40 compared to 10–15), and the relative intensities of the *a*-type transitions are also much larger than those for the *b*-type transitions. On the basis of this, we conclude that electrical anharmonicity is not a major contributor to the intensity of this overtone as it was for the oop bend as any unexpected intensity patterns are captured by the fixed charge model. The difference in the behaviors of the in- and out-of-plane bends reflects the fact that large displacements along θ_{ip} lead to the formation of a different hydrogen bond. In contrast, large-amplitude excursions in the oop bend coordinate effectively destroy the hydrogen bond.

We have also calculated the fundamental and first overtone for the singly deuterated complexes. Partial deuteration breaks the symmetry of the zero-point-corrected potential along the ip bend coordinate. This is illustrated in Figure 10B. In all cases, once zero-point energy in the other modes is included, the more stable isomer is the $X^- \cdot DOH$ isomer, which has a deuterium in the H_b position.¹⁶ This stability is reflected in the spectra in Figures 6 and 7, where both isomers are present, and the peaks attributed to the $X^- \cdot DOH$ isomer are larger than those assigned to the $X^- \cdot HOD$ isomer. Furthermore, analysis of the wave functions shows that although the barrier for isomerization is low, the wave functions can be characterized as having most of their amplitude in either the $X^- \cdot DOH$ or the $X^- \cdot HOD$ potential minima. This leads to two distinct progressions in the calculated spectra, as indicated in Tables 2, 4, and 5.

IVciv. In-Plane Bend + Water Bend Combination Bands.

While it is interesting to contrast the spectral signatures of the in- and out-of-plane bending motions, the transitions involving the ip bend discussed above are outside of the experimental frequency range, and there is consequently no way to compare these results directly with experiment. In considering where one might find signatures of the ip bend in the spectrum, we consider two observations. First, the OX^- stretch was only assigned in combination with the OH_b stretch. A rationalization for this is that the two vibrational modes can be considered as unequal admixtures of the OH_b and the X^-H_b stretching motions. Such a description has been discussed in more detail in ref 14. Likewise, as discussed above in the context of the HOD bend frequencies, the ip bend and water bend normal modes are actually unequal admixtures of these two zero-order modes. This is reflected in the isotope dependence of the ip bend harmonic frequencies. If θ_{ip} were a pure in-plane rotation of the water molecule, one would expect the frequency to be highest for $X^- \cdot H_2O$, intermediate and identical for $X^- \cdot HOD/X^- \cdot DOH$, and

lowest for $X^- \cdot D_2O$. In fact, the harmonic ip bend frequencies for $X^- \cdot HOD$ and $X^- \cdot DOH$ differ by as much as 13 cm^{-1} , with the frequency for $X^- \cdot DOH$ being the higher of the two.

On the basis of this, we looked for patterns in the spectra that could be attributed to the $\nu_{HOH} + \nu_{ip}$ combination bands. Such a band has already been tentatively assigned in the $Cl^- \cdot H_2O$ spectrum¹⁵ and is found at 1962 cm^{-1} in Figure 3. It was also assigned to a strong transition in the calculated $Cl^- \cdot H_2O$ spectrum of Rheinecker and Bowman.⁴¹ Taking the spacing between this combination band and the water bend fundamental (Figure 3) yields a value for ν_{ip} of 309 cm^{-1} . This value is in good agreement with the calculated fundamental frequency (333 cm^{-1}), reported in Table 4, and the line position is in even better agreement with the 1985 cm^{-1} calculated for this transition. In their six-dimensional calculations, Rheinecker and Bowman report the $Cl^- \cdot H_2O$ combination band at 2027 cm^{-1} , yielding an ip bend frequency that deviates from their calculated position for the fundamental band by only 5 cm^{-1} .⁴¹ The similarity between the ip bend frequencies evaluated when $n_{HOH} = 0$ and 1 can be explained by Figure 2C. Here, the frequency of the water bend is plotted as a function of the ip bend coordinate, and it varies little over $15 \leq \theta_{ip} \leq 60^\circ$, which is where the wave function has the most amplitude. This is exactly the region that is sampled by the vibrational wave functions when $n_{HOH} = 1$. As a result, the effective potentials, wave functions, and transition frequencies are similar when $n_{HOH} = 0$ and 1. On the basis of the above, it is not surprising that the shift of the $\nu_{HOH} + \nu_{ip}$ combination band from the ν_{HOH} fundamental provides a good approximation to the anharmonic frequency of the ip bend fundamental.

In analyzing the spectra in Figures 3–7, we find transitions that are assignable to this $\nu_{HOH} + \nu_{ip}$ combination band in many of the species and are indicated in orange. They are also labeled as band 3 in Figure 8. The experimental and calculated frequencies for these bands are reported in Tables 2 and 4, respectively. The calculated transitions occur as quartets in the $X^- \cdot H_2O$ and $X^- \cdot D_2O$ complexes, and we report all four frequencies. The splitting between the two pairs of states is generally smaller than 1 cm^{-1} , reflecting the small splitting of the ground-state tunneling doublet. The notable exception is $I^- \cdot H_2O$, where the splitting of the ground-state levels exceeds 4 cm^{-1} .

Overall, the agreement between experiment and calculation is very good. As is predicted in the calculations, the tunneling splitting increases from $Cl^- \cdot H_2O$ to $I^- \cdot H_2O$. This is reflected in the spectra shown in Figures 3–5. While in $Cl^- \cdot H_2O$ the $\nu_{HOH} + \nu_{ip}$ combination band appears as a single broad peak, in $I^- \cdot H_2O$, there are two resolvable features of nearly equal intensity, spaced by 91 cm^{-1} , compared to a theoretical value of 74 cm^{-1} . Preliminary results of calculations of the combination band intensities are consistent with the magnitudes relative to the ν_{HOH} bands seen in experiment.

V. Conclusion

In this paper, we have presented a complete set of spectra for the chloride-, bromide-, and iodide-water complexes, including partial and full deuteration of the water molecule. Spectra are reported for frequencies from ~ 800 to 3800 cm^{-1} . On the basis of the assignment of these spectra, transitions involving all six vibrational modes have been identified in the majority of the complexes. This provides a library with which one can investigate the role of anharmonicity, resonance interactions, and mode–mode coupling in these complexes.

Four-atom systems contain six vibrational degrees of freedom and are amenable to full-dimensional treatments of the molecular

vibrations. On the other hand, generation of six-dimensional potential surfaces that encompass all relevant regions of the potential and that are generated at a level of theory that is expected to produce spectroscopic accuracy is a large undertaking.^{41,42} Furthermore, as one moves from four-atom systems to larger complexes, for example, by introducing additional water molecules, generation of the potential surface and the calculations of the vibrational spectra in full dimensionality become increasingly challenging tasks. Consequently, a second goal of this work was to investigate how well reduced-dimensional treatments capture the spectral signatures of two of the intermolecular modes in these systems, specifically, the in- and out-of-plane bends. Finally, we discussed the qualitative implications of these results on the character and behavior of the anionic hydrogen bond.

As illustrated by the agreement between the experimental and calculated transition frequencies, the reduced-dimensional treatments of the two intermolecular bending coordinates can recover the observed behavior of these large-amplitude vibrational motions. In addition, by analyzing the results of our calculations, we were able to further probe the nature of the anomalously large electrical anharmonicities that are responsible for the large intensity of the overtone in the oop bend. We also predicted, and later verified by spectral assignment, splittings between the $\nu_{OH} + \nu_{ip}$ combination bands that increase in magnitude from chloride to bromide to iodide.

The larger goal of this work is to ask how the insights gained in these studies will aid in studies of spectra of larger complexes for which there are more vibrational modes and, consequently, the coupling among modes is necessarily stronger. This is an ongoing endeavor in studies of ion–water complexes. One important insight is the unexpectedly large intensity of the overtone of the mode that corresponds to displacement of hydrogen atoms involved in hydrogen bonds between the ion and the water molecule perpendicular to the bond axis. Similar signatures have been tentatively assigned for the $OH^- \cdot H_2O$ complex,²³ and we believe that they may be leading to previously unassigned transitions in spectra of other ion–water complexes. Likewise, the identification of the $\nu_{OH} + \nu_{ip}$ and $\nu_{OH} + \nu_{OX}$ combination bands in these complexes provides other targets for assignments in larger species.

Having discussed specific motions of these ion-solvated complexes, the questions become how general are they and what other insights do they provide into anion–water interactions, more generally. From a theoretical perspective, a change in the charge distribution of the solvent upon formation or loss of a hydrogen bond leads one to question the versatility of charge-centered models of solvents, in particular, water. From an experimental viewpoint, argon-tagged clusters provide a useful medium by which to study weakly bound ionic clusters and reactive intermediates, and spectroscopic studies of these types of systems can probe a variety of behaviors, such as the formation of and transfer between binding motifs, as well as charge density and charge-transfer information.^{24,25} Overall, such detailed studies, both experimentally and theoretically, can provide rich structural, energetic, electronic, and dynamical information about these complexes.

Acknowledgment. A.B.M. and M.A.J. would like to thank the chemistry division of the National Science Foundation for support of this work. This work was supported in part by an allocation of computing time from the Ohio Supercomputer Center to A.B.M. S.H. would also like to thank the Graduate School at The Ohio State University for fellowship support. We thank Timothy Guasco for his invaluable contributions in

refining the signal-to-noise ratio in the iodide monohydrate spectrum so as to clearly reveal the tunneling doublet. We acknowledge that the experimental data presented in this paper was only possible because of the pioneering efforts of Prof. W.C. Lineberger that led to the revolutionary and versatile pulsed ion beam methods central to the work. A.B.M., M.A.J., S.H., and G.H.W. would also like to thank Carl for his enthusiastic support and generously shared insights for this and many related studies over the years in our quest to understand the properties of cluster ions.

Supporting Information Available: Tables similar to Table 5 for the bromide and iodide complexes; comparisons of the fixed charge and full dipole surface calculations of the relative line strengths for the in- and out-of-plane bend for all 12 complexes; plots of the dependences of the OH bond lengths and OX^- distances for the in-plane bend scans; and plots of the fixed charge and full dipole surface calculations as functions of θ_{ip} and θ_{oop} for the H_2O complexes. This material is available free of charge via the Internet at <http://pubs.acs.org>.

References and Notes

- (1) Arrhenius, S. A. Z. *Phys. Chem.* **1887**, *1*, 631.
- (2) Knipping, E. M.; Lakin, M. J.; Foster, K. L.; Jungwirth, P.; Tobias, D. J.; Gerber, R. B.; Dabdub, D.; Finlayson-Pitts, B. J. *Science* **2000**, *288*, 301.
- (3) Tobias, D. J.; Jungwirth, P.; Parrinello, M. *J. Chem. Phys.* **2001**, *114*, 7036.
- (4) Jungwirth, P.; Tobias, D. J. *J. Phys. Chem. B* **2002**, *106*, 6361.
- (5) Roeselová, M.; Viece, J.; Dang, L. X.; Garrett, B. C.; Tobias, D. J. *J. Am. Chem. Soc.* **2004**, *126*, 16308.
- (6) Wang, H. S.; Pan, Z. M.; Shi, W. M.; Brown, B. S.; Wymore, R. S.; Cohen, I. S.; Dixon, J. E.; McKinnon, D. *Science* **1998**, *282*, 1890.
- (7) Miller, D. J.; Lisy, J. M. *J. Phys. Chem. A* **2007**, *111*, 12409.
- (8) Lybrand, P.; Kollman, P. A. *J. Chem. Phys.* **1985**, *83*, 2923.
- (9) Jorgensen, W. L.; Chandrasekhar, J.; Madura, J. D.; Impey, R. W.; Klein, M. L. *J. Chem. Phys.* **1983**, *79*, 926.
- (10) Hodges, M. P.; Stone, A. J.; Xantheas, S. S. *J. Phys. Chem. A* **1997**, *101*, 9163.
- (11) Wang, X.-B.; Werhahn, J. C.; Wang, L.-S.; Kowalski, K.; Laubereau, A.; Xantheas, S. S. *J. Phys. Chem. A* **2009**, *113*, 9579.
- (12) Corcelli, S. A.; Kelley, J. A.; Tully, J. C.; Johnson, M. A. *J. Phys. Chem. A* **2002**, *106*, 4872.
- (13) Ayotte, P.; Weddle, G. H.; Kim, J.; Johnson, M. A. *Chem. Phys.* **1998**, *239*, 485.
- (14) Horvath, S.; McCoy, A. B.; Roscioli, J. R.; Johnson, M. A. *J. Phys. Chem. A* **2008**, *112*, 12337.
- (15) Roscioli, J. R.; Diken, E. G.; Johnson, M. A.; Horvath, S.; McCoy, A. B. *J. Phys. Chem. A* **2006**, *110*, 4943.
- (16) Diken, E. G.; Shin, J.-W.; Price, E. A.; Johnson, M. A. *Chem. Phys. Lett.* **2004**, *387*, 17.
- (17) Kelley, J. A.; Weber, J. M.; Lisle, K. M.; Robertson, W. H.; Ayotte, P.; Johnson, M. A. *Chem. Phys. Lett.* **2000**, *327*, 1.
- (18) Ayotte, P.; Weddle, G. H.; Kim, J.; Kelley, J. A.; Johnson, M. A. *J. Phys. Chem. A* **1999**, *103*, 443.
- (19) Ayotte, P.; Weddle, G. H.; Kim, J.; Johnson, M. A. *J. Am. Chem. Soc.* **1998**, *120*, 12361.
- (20) Bailey, C. G.; Kim, J.; Dessent, C. E. H.; Johnson, M. A. *Chem. Phys. Lett.* **1997**, *269*, 122.
- (21) Ayotte, P.; Bailey, C. G.; Weddle, G. H.; Johnson, M. A. *J. Phys. Chem. A* **1998**, *102*, 3067.
- (22) Robertson, W. H.; Weddle, G. H.; Kelley, J. A.; Johnson, M. A. *J. Phys. Chem. A* **2002**, *106*, 1205.
- (23) Diken, E. G.; Headrick, J. M.; Roscioli, J. R.; Bopp, J. C.; Johnson, M. A.; McCoy, A. B.; Huang, X.; Carter, S.; Bowman, J. M. *J. Phys. Chem. A* **2005**, *109*, 571.
- (24) Shin, J.-W.; Hammer, N. I.; Diken, E. G.; Johnson, M. A.; Walters, R. S.; Jaeger, T. D.; Duncan, M. A.; Christie, R. A.; Jordan, K. D. *Science* **2004**, *304*, 1137.
- (25) Relf, R. A.; Guasco, T. L.; Elliott, B. M.; Kamrath, M. Z.; McCoy, A. B.; Steele, R. P.; Schofield, D. P.; Jordan, K. D.; Viggiano, A. A.; Ferguson, E. E.; Johnson, M. A. *Science* **2010**, in press.
- (26) Johnson, M. A.; Lineberger, W. C. Pulsed Methods for Cluster Ion Spectroscopy. In *Techniques for the Study of Ion–Molecule Reactions*; Farrar, J. M., Saunders, W. H., Jr., Ed.; Wiley: New York, 1988; Vol. XX, pp 591.

- (27) Posey, L. A.; DeLuca, M. J.; Johnson, M. A. *Chem. Phys. Lett.* **1986**, *131*, 170.
- (28) Frisch, M. J.; Trucks, G. W.; Schlegel, H. B.; Scuseria, G. E.; Robb, M. A.; Cheeseman, J. R.; Montgomery, J. A., Jr.; Vreven, T.; Kudin, K. N.; Burant, J. C.; Millam, J. M.; Iyengar, S. S.; Tomasi, J.; Barone, V.; Mennucci, B.; Cossi, M.; Scalmani, G.; Rega, N.; Petersson, G. A.; Nakatsuji, H.; Hada, M.; Ehara, M.; Toyota, K.; Fukuda, R.; Hasegawa, J.; Ishida, M.; Nakajima, T.; Honda, Y.; Kitao, O.; Nakai, H.; Klene, M.; Li, X.; Knox, J. E.; Hratchian, H. P.; Cross, J. B.; Bakken, V.; Adamo, C.; Jaramillo, J.; Gomperts, R.; Stratmann, R. E.; Yazyev, O.; Austin, A. J.; Cammi, R.; Pomelli, C.; Ochterski, J. W.; Ayala, P. Y.; Morokuma, K.; Voth, G. A.; Salvador, P.; Dannenberg, J. J.; Zakrzewski, V. G.; Dapprich, S.; Daniels, A. D.; Strain, M. C.; Farkas, O.; Malick, D. K.; Rabuck, A. D.; Raghavachari, K.; Foresman, J. B.; Ortiz, J. V.; Cui, Q.; Baboul, A. G.; Clifford, S.; Cioslowski, J.; Stefanov, B. B.; Liu, G.; Liashenko, A.; Piskorz, P.; Komaromi, I.; Martin, R. L.; Fox, D. J.; Keith, T.; Al-Laham, M. A.; Peng, C. Y.; Nanayakkara, A.; Challacombe, M.; Gill, P. M. W.; Johnson, B.; Chen, W.; Wong, M. W.; Gonzalez, C.; Pople, J. A. *Gaussian 03*, revision C.02; Gaussian, Inc.: Wallingford, CT, 2004.
- (29) Peterson, K. A.; Shepler, B. C.; Figgen, D.; Stoll, H. *J. Phys. Chem. A* **2006**, *110*, 13877.
- (30) Peterson, K. A.; Figgen, D.; Goll, E.; Stoll, H.; Dolg, M. *J. Chem. Phys.* **2003**, *119*, 11113.
- (31) Dunning, T. H. *J. Phys. Chem. A* **2000**, *104*, 9062.
- (32) Eckart, C. *Phys. Rev.* **1935**, *47*, 552.
- (33) Louck, J. D.; Galbraith, H. G. *Rev. Mod. Phys.* **1976**, *48*, 69.
- (34) Miller, W. H.; Handy, N. C.; Adams, J. E. *J. Chem. Phys.* **1980**, *72*, 99.
- (35) Fehrens, B.; Luckhaus, D.; Quack, M. *Chem. Phys. Lett.* **1999**, *300*, 312.
- (36) Frederick, J. H.; Woywod, C. *J. Chem. Phys.* **1999**, *111*, 7255.
- (37) Wilson, E. B. *J. Chem. Phys.* **1939**, *7*, 1047.
- (38) Vendrell, O.; Gatti, F.; Meyer, H.-D. *J. Chem. Phys.* **2007**, *127*, 184303.
- (39) Vendrell, O.; Gatti, F.; Lauvergnat, D.; Meyer, H. D. *J. Chem. Phys.* **2007**, *127*, 184302.
- (40) Vendrell, O.; Meyer, H. D. *Phys. Chem. Chem. Phys.* **2008**, *10*, 4692.
- (41) Rheinecker, J.; Bowman, J. M. *J. Chem. Phys.* **2006**, *125*, 133206.
- (42) Rheinecker, J. L.; Bowman, J. M. *J. Chem. Phys.* **2006**, *124*, 131102.
- (43) Herzberg, G. *Molecular Spectra and Molecular Structure II. Infrared and Raman Spectra of Polyatomic Molecules*; Van Nostrand Reinhold Company Inc.: New York, 1945; Vol. II.
- (44) Shimanouchi, T. Molecular Vibrational Frequencies. In *NIST Chemistry WebBook, NIST Standard Reference Database Number 69*; Linstrom, P. J., Mallard, W. G. Eds.; National Institute of Standards and Technology: Gaithersburg, MD, <http://webbook.nist.gov> (retrieved September 1, 2009).
- (45) Foster, J. P.; Weinhold, F. *J. Am. Chem. Soc.* **1980**, *102*, 7211.
- (46) Carpenter, J. E.; Weinhold, F. *J. Mol. Struct.: THEOCHEM* **1988**, *169*, 41.

JP9088782